A Comparative Analysis of Localized and Propagating Surface Plasmon Resonance Sensors: The Binding of Concanavalin A to a Monosaccharide Functionalized Self-Assembled Monolayer

Chanda Ranjit Yonzon,[†] Eunhee Jeoung,[‡,§] Shengli Zou,[†] George C. Schatz,[†] Milan Mrksich,[‡] and Richard P. Van Duyne*,[†]

Contribution from the Department of Chemistry, Northwestern University, 2145 Sheridan Road, Evanston, Illinois 60208-3113, and Department of Chemistry and The Institute for Biophysical Dynamics, The University of Chicago, Chicago, Illinois 60637

Received May 17, 2004; E-mail: vanduyne@chem.northwestern.edu

Abstract: A comparative analysis of the properties of two optical biosensor platforms: (1) the propagating surface plasmon resonance (SPR) sensor based on a planar, thin film gold surface and (2) the localized surface plasmon resonance (LSPR) sensor based on surface confined Ag nanoparticles fabricated by nanosphere lithography (NSL) are presented. The binding of Concanavalin A (ConA) to mannose-functionalized self-assembled monolayers (SAMs) was chosen to highlight the similarities and differences between the responses of the real-time angle shift SPR and wavelength shift LSPR biosensors. During the association phase in the real-time binding studies, both SPR and LSPR sensors exhibited qualitatively similar signal vs time curves. However, in the dissociation phase, the SPR sensor showed an approximately 5 times greater loss of signal than the LSPR sensor. A comprehensive set of nonspecific binding studies demonstrated that this signal difference was not the consequence of greater nonspecific binding to the LSPR sensor but rather a systematic function of the Ag nanoparticle's nanoscale structure. Ag nanoparticles with larger aspect ratios showed larger dissociation phase responses than those with smaller aspect ratios. A theoretical analysis based on finite element electrodynamics demonstrates that this results from the characteristic decay length of the electromagnetic fields surrounding Ag nanoparticles being of comparable dimensions to the ConA molecules. Finally, an elementary (2×1) multiplexed version of an LSPR carbohydrate sensing chip to probe the simultaneous binding of ConA to mannose and galactose-functionalized SAMs has been demonstrated.

Introduction

Remarkable progress has been made in the last two decades in the development of optical biosensors and their application in environmental protection,[1,2] biotechnology,[3] medical diagnostics,[4] drug screening,[5] food safety,[2,6] and security.[7] The potential of surface plasmon resonance (SPR) biosensors was realized in the early 1980s by Liedberg et al., who were able to sense immunoglobulin antibodies by observing the change in the critical angle when the antibodies bound selectively to a Au film.[8] SPR sensors have been used to study many kinds of ligand−receptor interactions including protein−ligand,[9] antibody−antigen,[10] protein−carbohydrate,[11,12] protein−DNA,[13] DNA−DNA,[14] and cell adhesion[15] interactions. Recently, the first antibody biosensing based on measurements of extinction changes caused by perturbation of the local refractive index on colloidal Au nanoparticles was reported.[16] Since then, nanoparticle-based LSPR sensors have been increasingly used for biological[17−20] and chemical sensing.[21,22]

† Northwestern University.

‡ The University of Chicago.

§ Present address: Department of Chemistry, Kangnung University National University, Gangwondo, Korea.

(1) Ji, J.; Schanzle, J. A.; Tabacco, M. B. *Anal. Chem.* **2004**, *76*, 1411−1418.
(2) Ligler, F. S.; Taitt, C. R.; Shriver-Lake, L. C.; Sapsford, K. E.; Shubin, Y.; Golden, J. P. *Anal. Bioanal. Chem.* **2003**, *377*, 469−477.
(3) Kohls, O.; Scheper, T. *Sens. Actuators, B* **2000**, *70*, 121−130.
(4) Yonzon, C. R.; Haynes, C. L.; Zhang, X.; Walsh, J. T.; Van Duyne, R. P. *Anal. Chem.* **2004**, *76*, 78−85.
(5) Ho, H.; Leclerc, M. *J. Am. Chem. Soc.* **2004**, *126*, 1384−1387.
(6) Wiskur, S. L.; Anslyn, E. V. *J. Am. Chem. Soc.* **2001**, *123*, 10109−10110.
(7) Bauer, G.; Hassmann, J.; Walter, H.; Haglmueller, J.; Mayer, C.; Schalkhammer, T. *Nanotech.* **2003**, 1289−1311.
(8) Liedberg, B.; Nylander, C.; Lundstorm, I. *Sens. Actuators, B* **1983**, *4*, 229−304.

(9) Mrksich, M.; Grunwell, J. R.; Whitesides, G. M. *J. Am. Chem. Soc.* **1995**, *117*, 12009−12010.
(10) Berger, C. E. H.; Beumer, T. A. M.; Kooyman, R. P. H.; Greve, J. *Anal. Chem.* **1998**, *70*, 703−706.
(11) MacKenzie, C. R.; Hirama, T.; Deng, S. j.; Bundle, D. R.; Narang, S. R. *J. Biol. Chem.* **1996**, *271*, 1527−1533.
(12) Mann, D. A.; Kanai, M.; Maly, D. J.; Kiessling, L. L. *J. Am. Chem. Soc.* **1998**, *120*, 10575−10582.
(13) Brockman, J. M.; Frutos, A. G.; Corn, R. M. *J. Am. Chem. Soc.* **1999**, *121*, 8044−8051.
(14) Gotoh, M.; Hasegawa, Y.; Shinohara, Y.; Shimizu, M.; Tosu, M. *DNA Res.* **1995**, *2*, 285−293.
(15) Van Der Merwe, P. A.; Barclay, A. N. *Curr. Opin. Immunol.* **1996**, *8*, 257−261.
(16) Englebienne, P. *Analyst* **1998**, *123*, 1599−1603.
(17) Riboh, J. C.; Haes, A. J.; McFarland, A. D.; Yonzon, C. R.; Van Duyne, R. P. *J. Phys. Chem. B* **2003**, *107*, 1772−1780.
(18) Yonzon, C. R.; Zhang, X.; Van Duyne, R. P. *Proc. SPIE* **2003**, *5224*, 78−85.

Propagating surface plasmons are evanescent electromagnetic waves bounded by flat smooth metal-dielectric interfaces and arise from oscillations of the conduction electrons in the metal.[23] When surface plasmons are confined on periodic,[24] colloidal,[21] or other nanosystems,[25] localized optical modes are observed. These optical modes lead to highly localized electromagnetic fields outside the particles. Both SPR and LSPR are sensitive to the local refractive index changes that occur when the target analyte binds to the metal film or nanoparticles. Surface refractive index sensors have an inherent advantage over optical biosensors that require a chromophoric group or other label to transduce the binding event. Furthermore, they require very little ligand purification due to the specific ligand/receptor binding of these sensors. Also, these sensors provide real-time information on the course of binding and are applicable over a broad range of binding affinities. Additionally, LSPR sensing elements are inherently the size of a single nanoparticle, making the LSPR sensors potentially applicable for in situ detection in biological systems. The sensing capability of LSPR sensors can also be tuned by changing the shape, size, and material composition of the nanoparticles.[26,27]

Herein, we describe comparative sensor studies conducted on the specific interactions between carbohydrates and proteins using both conventional propagating SPR and the newly developed LSPR sensors. The functions and dynamics of carbohydrate/protein interactions in biology have been characterized in a variety of processes, including cell adhesion,[28] immunity,[29] and development.[30] Rapid and parallel screening of biomolecular interactions is necessary to understand the biological functions of carbohydrates and carbohydrate binding proteins. One way to achieve this screening is to immobilize the sugars of interest on a sensing surface in an array format, which is then exposed to a protein solution. Array-based sensors have several advantages including low consumption of analytes, the ability to perform parallel screening of multiple interactions, and efficient response readout.[31] Chips that present arrays of many different carbohydrates will be important for identifying proteins and enzymes that interact with sugars and, therefore, will be valuable tools for understanding glycomics.[32−35] We have shown the immobilization of carbohydrates on a flat Au surface and specific binding of Concanavalin A (ConA) using SPR sensors on carbochips.[36]

ConA is a 104 kDa mannose specific plant lectin comprised of a tetramer with dimensions of 63.2, 86.9, and 89.3 Å and has four binding sites.[37] Previously, the surface binding constant for ConA to a mannose-functionalized self-assembled monolayer (SAM) was found to be 5.6×10^6 M^{-1} by SPR imaging studies.[38] The present work demonstrates (1) the real-time binding of ConA to a mannose-functionalized SAM using both SPR and LSPR sensors, (2) comprehensive nonspecific binding studies to ensure that the signal transduction was due to the specific binding of ConA, (3) depth-profiling analysis of the real-time LSPR dissociation responses when ConA binds to the mannose-functionalized surface, (4) theoretical modeling to understand the change in the LSPR dissociation response with respect to the aspect ratios of the Ag nanoparticles, and (5) the first step toward fabricating a multiplexed carbohydrate sensing chip−LSPR sensor.

Methods

Materials. Ag (99.99%) was purchased from D. F. Goldsmith (Evanston, IL), and Au (99.99%) was acquired from Materials Research (Orangeburg, NY). Tungsten vapor deposition boats were purchased from R. D. Mathis (Long Beach, CA). Mica substrates were obtained from Asheville-Schoonmaker (Newport News, VA) and were die-punched into 18-mm diameter disks. Glass substrates were 18-mm diameter, no. 2 coverslips from Fisher Scientific (Fairlawn, VA). Pretreatment of glass substrates required H_2SO_4, H_2O_2, and NH_4OH, which were obtained from Fisher Scientific (Fairlawn, VA). Surfactant-free, white carboxyl-substituted polystyrene latex nanospheres with diameters of 390 nm ± 19.5 nm were received as a suspension in water from Duke Scientific (Palo Alto, CA). Ti was purchased from Aldrich (Milwaukee, WI). Phosphate buffered saline (PBS), pH = 7.4 was obtained from Sigma (St. Louis, MO). Absolute ethanol was purchased from Pharmco (Brookfield, CT).

Synthesis. The compounds 11-mercaptoundecyl tri(ethyelene glycol) disulfide (EG3), **1**, malemide terminated disulfide, **2**, mannose thiol, **3** (Figure 1C), and galactose thiol were synthesized as described in the literature.[39]

Nanosphere Lithography (NSL). Glass substrates were pretreated in two steps: (1) piranha etch, 1:3 30% H_2O_2/H_2SO_4 at 80 °C for 0.5 h to clean the substrate and (2) base treatment, 5:1:1 H_2O/NH_4OH: 30% H_2O_2 with sonication for 1 h, which rendered the surface hydrophilic. Both piranha etch and base treatment were done in the hood with appropriate safety goggles and lab coats. Mica substrates were cut into 18-mm diameter disks and freshly cleaved immediately prior to use. Approximately 2 μL and 10 μL of undiluted nanosphere solution (10% solid) were drop-coated on the pretreated glass and mica substrates, respectively. The nanospheres were allowed to dry in ambient conditions to form a 2D hexagonally close-packed array. Ag was deposited in a modified Consolidated Vacuum Corporation vapor deposition system with a base pressure of 10^{-7} Torr. The mass thickness and deposition rate (1 Å/sec) for each film were measured using a Leybold Inficon XTM/2 quartz-crystal microbalance (East Syracuse, NY). After Ag deposition, the sphere mask was removed by sonication in absolute ethanol for 3 min.

SPR and LSPR Sensor Fabrication and Experimental Protocol. For the SPR sensor, Au (50 nm) was evaporated on glass coverslips with a thin Ti underlayer (10 nm), and for the LSPR sensors, NSL created Ag nanoparticle arrays were used. The SAM was prepared by

(19) Raschke, G.; Kowarik, S.; Franzl, T.; Sönnichsen, C.; Klar, T. A.; Feldmann, J.; Nichtl, A.; Kürzinger, K. *Nano Lett.* **2003**, *3*, 935−938.
(20) Haes, A. J.; Van Duyne, R. P. *J. Am. Chem. Soc.* **2002**, *124*, 10596−10604.
(21) McFarland, A. D.; Van Duyne, R. P. *Nano Lett.* **2003**, *3*, 1057−1062.
(22) Zhang, H.-L.; Evans, S. D.; Henderson, J. R.; Miles, R. E.; Shen, T.-H. *Nanotech.* **2002**, *13*, 439−444.
(23) Reather, H. *Surface Polaritons on Smooth and Rough Surfaces and on Gratings*; Springer-Verlag: Berlin, 1988.
(24) Garcia-Vidal, F. J.; Pendry, J. B. *Phys. Rev. Lett.* **1996**, *77*, 1163−1666.
(25) Jensen, T. R.; Schatz, G. C.; Van Duyne, R. P. *J. Phys. Chem. B* **1999**, *103*, 2394−2401.
(26) Haynes, C. L.; Van Duyne, R. P. *J. Phys. Chem. B* **2001**, *105*, 5599−5611.
(27) Haes, A. J.; Zou, S.; Schatz, G. C.; Van Duyne, R. P. *J. Phys. Chem. B* **2004**, *108*, 109−116.
(28) Kannagi, R. *Glycoconjugate J.* **1997**, *14*, 577−584.
(29) Feizi, T. *Immunol. Rev.* **2000**, *173*, 79−88.
(30) Dennis, J. W.; Granovsky, M.; Warren, C. E. *BioEssays* **1999**, *21*, 412−421.
(31) Smith, E. A.; Corn, R. M. *Appl. Spectrosc.* **2003**, *57*, 320A−332A.
(32) Kiessling, L. L.; Cairo, C. W. *Nat. Biotech.* **2002**, *20*, 234−235.
(33) Wang, D.; Liu, S.; Trummer, B. J.; Deng, C.; Wang, A. *Nat. Biotech.* **2002**, *20*, 275−281.
(34) Fukui, S.; Feizi, T.; Galustian, C.; Lawson, A. M.; Chai, W. *Nat. Biotech.* **2002**, 1011−1017.
(35) Fazio, F.; Bryan, M. C.; Blixt, O.; Paulson, J. C.; Wong, C. *J. Am. Chem. Soc.* **2002**, *124*, 14397−14402.
(36) Houseman, B. T.; Mrksich, M. *Chem. Biol.* **2002**, *9*, 443−454.
(37) Hardman, K. D.; Ainsworth, C. F. *Biochemistry* **1972**, *11*, 4910−4919.
(38) Smith, E. A.; Thomas, W. D.; Kiessling, L. L.; Corn, R. M. *J. Am. Chem. Soc.* **2003**, *125*, 6140−6148.
(39) Houseman, B. T.; Gawalt, E. S.; Mrksich, M. *Langmuir* **2003**, *19*, 1522−1531.
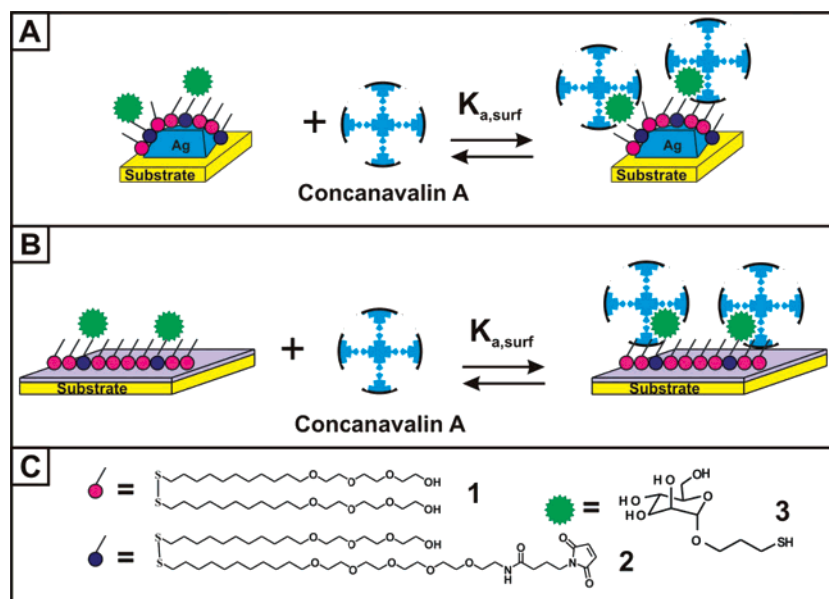
Figure 1. Schematic representation of Concanavalin A (ConA) binding to a mannose-functionalized (A) Ag nanosensor fabricated by NSL and (B) Au SPR sensor. (C) Structures of (1) 11-mercaptoundecyl tri(ethylene glycol) disulfide (EG3), (2) malemide-terminated disulfide, and (3) mannose thiol.

immersing the coverslips in an ethanolic solution containing 450 μL of tri(ethylene glycol) disulfide, **1** (1 mM), and 50 μL maleimide-terminated disulfide, **2** (1 mM). After 12 h, the coverslips were rinsed with ethanol and dried under a stream of nitrogen. The substrates presenting maleimide-functional groups were immersed in methanolic solutions of 5 mM mannose thiol, **3**, for 40 min. The mannose thiol covalently binds to **2**, providing ∼5% sugar-immobilized surfaces, based on the fraction of starting thiols and efficiency of the malemide reaction.[40] The mannose-functionalized sensors were then exposed to ConA for 20 min (Figure 1A, B). The actual surface coverage of the SAM has not been measured; however, maximum response of ConA binding occurs under these conditions.

Atomic Force Microscopy (AFM). AFM was used to obtain topographic images of the nanoparticle arrays. The images were taken under ambient conditions with a Digital Instruments Nanoscope IV microscope with a Nanoscope IIIa controller operating in tapping mode. Etched Si nanoprobe tips from Digital Instruments (Santa Barbara, CA) were used to image the sample. These tips had resonance frequencies between 280 and 320 kHz and were conical in shape, with a cone angle of 20° and an effective radius of curvature of 10 nm at the tip.

Surface Plasmon Resonance Spectroscopy. A BIACore 1000 (Neuchâtel, Switzerland) was used for all propagating SPR measurements reported here. The mannose-functionalized substrate was incorporated into BIAcore cassettes by gluing the chip into the cassettes using a Devcon two-part epoxy (Danvers, MA). PBS, pH 7.4, was used as the running buffer, and measurements were reported as changes in resonance angle ($\Delta\theta$), where 1° = 10 000 RU.

Localized Surface Plasmon Resonance (LSPR) Spectroscopy. LSPR extinction measurements were taken using an Ocean Optics (Dunedin, FL) SD2000 fiber optically coupled spectrometer. All spectra in this study were from macroscopic measurements obtained in transmission mode using unpolarized white light with a probe diameter of ∼2 mm. A home-built flow cell was used to control the surrounding environment of the Ag nanoparticles and to introduce the analytes.[41]

Results and Discussion

LSPR Response to Mannose-Functionalized Ag Nanoparticles. The Ag LSPR nanosensor was rinsed with ethanol and placed in a flow cell after incubation in mannose. The LSPR spectrum of the mannose-functionalized Ag nanosensor in N_2 had a λ_{max} of 636.5 nm (Figure 2A). Then, 19.8 μM Con A
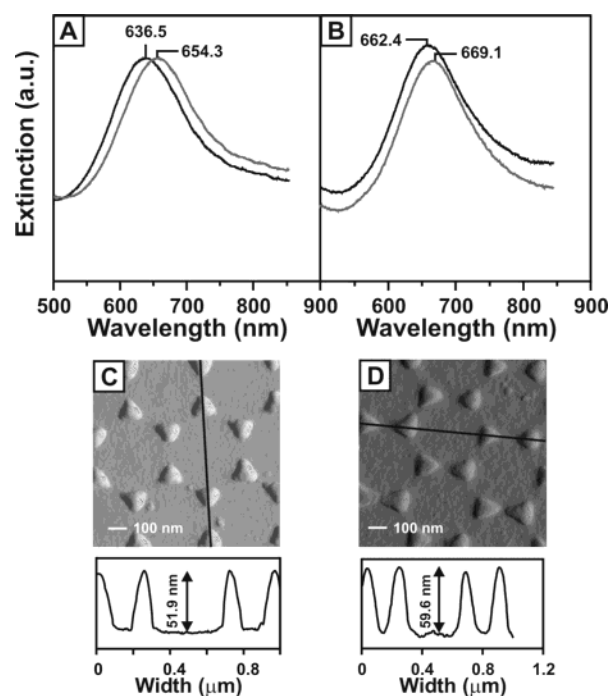
Figure 2. (A) LSPR spectra of mannose-functionalized Ag nanosensor (λ_{max} = 636.5 nm) and the specific binding of ConA (λ_{max} = 654.3 nm) in nitrogen. (B) LSPR spectra of mannose-functionalized Ag nanobiosensor (λ_{max} = 662.4 nm) and the specific binding of ConA to mannose (λ_{max} = 669.1) in PBS buffer. (C) Tapping mode AFM image of mannose-functionalized Ag nanobiosensor (nanosphere diameter, D = 390 nm; Ag thickness, d_m = 50 nm; scan rate = 2 Hz; scan size 1 μm). The mannose-functionalized Ag nanobiosensor with an average height of 51.9 nm. (D) Tapping mode AFM image of Ag nanobiosensor after specific binding of ConA (19 μM) with an average height of 59.6 nm.

was injected into the flow cell, and the Ag nanosensor was incubated at room temperature for 20 min. The sample was thoroughly rinsed in buffer solution, and the LSPR λ_{max} of the

(40) Folkers, J. P.; Laibinis, P. E.; Whitesides, G. M. *J. Phys. Chem* **1994**, *98*, 563−571.
(41) Malinsky, M. D.; Kelly, K. L.; Schatz, G. C.; Van Duyne, R. P. *J. Am. Chem. Soc.* **2001**, *123*, 1471−1482.
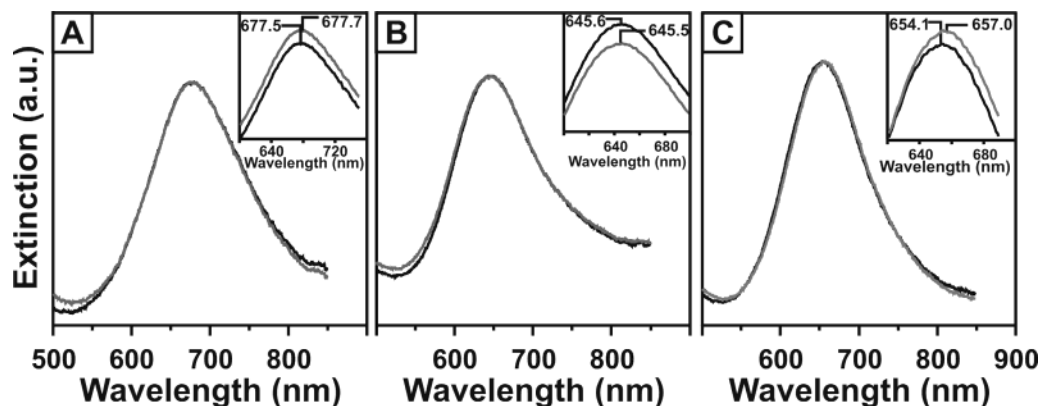
Figure 3. Nonspecific binding study on mannose-functionalized Ag nanosensor with two different proteins. All extinction measurements were taken in PBS buffer. All insets magnify the extinction spectra, and the λ_{max} are denoted. (A) LSPR spectra illustrating nonspecific binding of Ery (26 μM) to the mannose-functionalized surface. (B) LSPR spectra illustrating nonspecific binding of bovine serum albumin (29 μM) to the mannose-functionalized surface. (C) LSPR spectra illustrating binding of ConA (9.6 μM) in the presence of BSA (15 μM).

Ag nanotriangles was measured to be 654.3 nm, resulting in a 17.8-nm red-shift. The LSPR response ($\Delta\lambda_{max}$) seen when ConA binds to the mannose-functionalized surface has been previously described using the following equation:[17]

$$\Delta\lambda_{max} = m\theta(n_{ConA} - n_{environment}) \exp(-2d_{SAM}/l_d)[1 - \exp(-2d_{ConA}/l_d)] \quad (1)$$

where m is the refractive index sensitivity of the Ag nanosensor ($m = 191$ nm per refractive index unit for Ag nanoparticles with an in-plane width of $\sim$100 nm and out-of-plane height of 50 nm),[41] θ is the ConA surface coverage (for full surface coverage, $\theta = 1$), n_{ConA} is the refractive index of ConA, $n_{environment}$ is the refractive index of the environment in the cell ($n_{environment} = 1$ for N$_2$, $n_{environment} = 1.33$ for buffer, $n_{ConA} = 1.57$),[42] d_{SAM} is the thickness of EG3 layer ($d_{SAM} = 2$ nm),[43] d_{ConA} is the thickness of ConA, and l_d (l_d = electromagnetic field decay length) is the characteristic l_d of the Ag nanosensor ($l_d \approx 5-6$ nm for Ag nanoparticles with an in-plane width of $\sim$100 nm and out-of-plane height of 50 nm).[20]

The LSPR response of ConA binding to the mannose-functionalized on a Ag nanosensor was also measured directly in a buffer environment resulting in a 6.7-nm red-shift (Figure 2B). The 60% reduction of signal in buffer relative to the N$_2$ environment is predicted by eq 1 and has been previously observed.[17] The binding of ConA to mannose-functionalized surfaces was confirmed by height changes in AFM measurements (Figure 2D, E). The average height of the mannose-functionalized Ag nanoparticles was measured to be 51.9 nm (Figure 2D). After ConA incubation, the average nanoparticle height was 59.6 nm (Figure 2E), an increase of 7.7 nm. This result corresponds to the thickness of a monolayer of ConA as estimated from its X-ray structure.[37]

Nonspecific Binding Studies. A viable nanosensor should have very few nonspecific interactions. To verify that the LSPR response seen when ConA binds to the mannose functionalized surface is due primarily to specific binding between the ligand and the receptor, the following nonspecific binding studies were performed: (1) erythrina crystagalli (Ery) interacting with the mannose-functionalized surface sensor, (2) bovine serum albumin (BSA) interacting with the mannose-functionalized surface, and (3) mixtures of bovine serum albumin and ConA interacting with the mannose-functionalized surface (Figure 3). For all the

nonspecific binding studies, Ag nanoparticles with an in-plane width of $\sim$100 nm and out-of-plane height equal to 50 nm were used. The absolute LSPR λ_{max} of these nanoparticles vary from sample to sample due to formation of an adsorbed water layer and the slight natural structural variance of the NSL-fabricated Ag nanoparticles. In previous work, it was demonstrated that the LSPR λ_{max} shift is not a function of its absolute position.[17,20,41] All measurements were taken in buffer and the insets magnify the LSPR λ_{max}.

(1) Erythrina Crystagalli (Ery) Interacting with the Mannose-Functionalized Sensor. Ery is a dimer plant lectin with a molecular weight of 56 kDa that specifically binds to galactose.[44] The Ag nanosensors were exposed to Ery to demonstrate that the mannose-functionalized Ag nanosensors do not have an affinity toward lectins other than mannose binding lectins. The Ag nanosensors functionalized with mannose SAMs had an LSPR λ_{max} of 677.5 nm (Figure 3A). Incubation of the sensor in 26 μM Ery for 20 min resulted in an LSPR λ_{max} of 677.7 nm. The 0.2-nm shift corresponds to the instrumental noise wavelength shift in the baseline, illustrating that lectins not specific to mannose do not bind to the mannose-functionalized sensor surface.

(2) BSA Interacting with the Mannose-Functionalized Sensor. The Ag nanosensors were exposed to a BSA solution to demonstrate that they neither have an affinity toward other lectins nor interact with other proteins. The Ag nanoparticles were functionalized with mannose thiols giving an LSPR λ_{max} of 645.6 nm (Figure 3B). Incubation of the sensor in 29 μM BSA for 20 min resulted in an LSPR λ_{max} of 645.5 nm, which too is equal to the instrumental noise.

(3) Specific Sensing in the Presence of Interfering Protein. While the Ag nanosensor shows no affinity toward other proteins, it is critical to show specific ConA binding in the presence of interfering proteins. The mannose-functionalized Ag nanonsensor (LSPR $\lambda_{max} = 654.1$ nm) was incubated with a mixture of 9.6 μM ConA and 15 μM BSA giving an LSPR λ_{max} of 657.0 nm, resulting in a 2.9-nm red-shift. The 3.1-nm red-shift seen in this experiment is a necessary but not sufficient

(42) Jung, L. S.; Campbell, C. T.; Chinowsky, T. M.; Mar, M. N.; Yee, S. S. *Langmuir* **1998**, *14*, 5636–5648.
(43) Palegrosdemange, C.; Simon, E. S.; Prime, K. L.; Whitesides, G. M. *J. Am. Chem. Soc.* **1991**, *113*, 12–20.
(44) Gupta, D.; Cho, M.; Cummings, R. D.; Brewer, C. F. *Biochemistry* **1996**, *35*, 15236–15243.
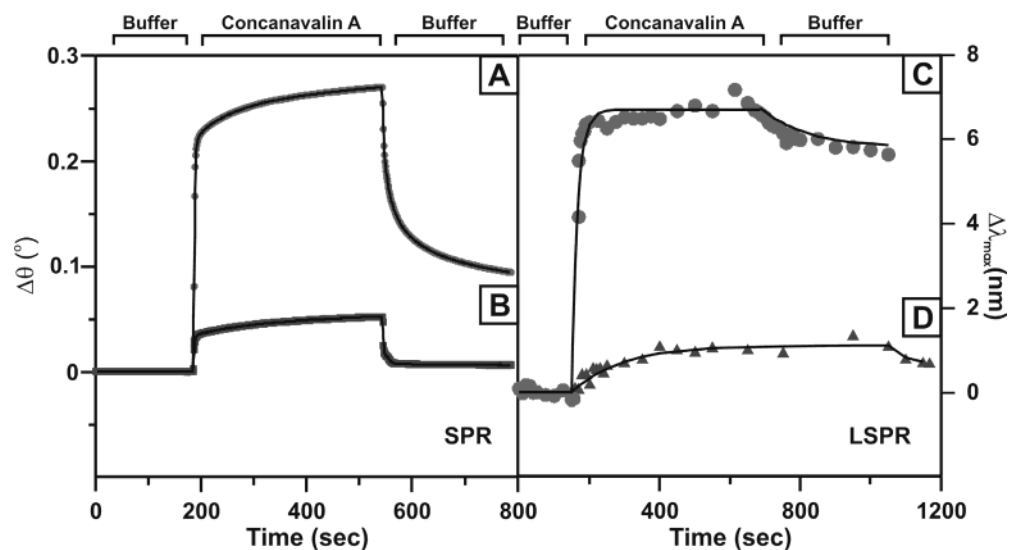
Figure 4. Real-time response of sugar-functionalized sensor as 19 μM of ConA was injected in the cell following buffer injection. (A) mannose-functionalized SPR sensor, (B) galactose-functionalized SPR sensor, (C) mannose-functionalized Ag nanosensor, and (D) galactose-functionalized Ag nanosensor. The points are the experimental data. The solid line for the SPR measurement is composed of straight line segments connecting the experimental data. The solid line in LSPR measurement is a first-order adsorption kinetics fit to the data and should only be interpreted as a guide to the eye.

result to demonstrate the specificity of ConA binding to the mannose-functionalized Ag nanosensor. Further confirmation awaits the measurement of the LSPR response at a fixed concentration of ConA, near the midpoint of the binding curve, in the presence and absence of BSA. The LSPR shifts seen in these experiments demonstrate the specificity of ConA binding to the mannose-functionalized Ag nanosensor.

In addition, a nonspecific binding study of ConA using a sensor without covalently linked sugar was also performed (data not shown). This experiment demonstrated that the nanosensor without any sugar on the surface shows no affinity toward ConA. The aforementioned results have demonstrated that the LSPR Ag nanosensor shows no nonspecific binding toward other proteins and binds to ConA even in the presence of interfering proteins, demonstrating viability of the nanosensor.

Real-Time Binding Studies. To compare the real-time response of the flat surface SPR sensor (Figure 4A) and the LSPR Ag nanosensor (Figure 4C), the SPR response ($\Delta\theta$) and LSPR $\Delta\lambda_{max}$ response to the ConA binding on the mannose-functionalized surface was investigated. After the baseline SPR $\Delta\theta$ response of the mannose-functionalized Au surface in a running buffer environment was recorded, 19 μM ConA in buffer was injected. The sensor was then flushed with buffer for removal of nonspecifically bound ConA and a partial dissociation of ConA bound as the 1:1 mannose complex. Figure 4A illustrates the real-time monitoring of 19 μM ConA by the SPR $\Delta\theta$ shift. Similarly, the real-time LSPR response of ConA binding to the mannose-functionalized Ag nanonsensor was also probed. After the LSPR λ_{max} of the mannose-functionalized surface was recorded, 19 μM ConA was manually injected in the flow cell, and then the sample was flushed with PBS buffer. During this process, the LSPR λ_{max} was measured in 5-s intervals for 20 min (Figure 4C). Note that the spike of $\Delta\lambda_{max}$ at 500 s in Figure 4C is caused by flow nonuniformity (noise) due to manual injection.

During the association phase, both the SPR and LSPR sensor showed a rapid response when ConA was exposed to the surface, which indicates strong 1:1 mannose/ConA binding on the

surface[38] followed by weak nonspecific binding. However, during the dissociation phase, when the ConA-bound SPR sensor surface was flushed with PBS buffer, the response decreased by 60% whereas the response of the LSPR sensor decreased only by 14%. Our working hypothesis to explain this difference is the longer decay length of the SPR sensor's electromagnetic field ($l_d \approx 200$ nm),[42] compared to that of the LSPR sensor ($l_d \approx 5-6$ nm).[20] The dissociation response seen in the SPR sensor is caused by removal of nonspecifically bound ConA, partial dissociation of 1:1 bound ConA with mannose, and change in bulk refractive index from ConA/buffer to only buffer.[39] However, due to a shorter decay length of the electromagnetic field of the LSPR sensor, the dissociation response seen can be attributed only to removal of nonspecifically bound ConA and partial dissociation of bound ConA.

A similar real-time experiment was performed to observe the binding of ConA to a galactose-functionalized planar Au sensor (Figure 4B) and Ag nanosensor (Figure 4D). To illustrate that ConA has very little affinity toward galactose, 5% galactose-functionalized surface was exposed to 19 μM ConA. After the wash with PBS buffer, both SPR and LSPR sensors showed very small $\Delta\theta$ or $\Delta\lambda_{max}$. This small response was previously observed when fluorescently labeled ConA was exposed to a galactose-functionalized surface.[39]

Understanding the Dissociation Phase Response of the LSPR Nanosensor. To understand why the dissociation phase signal in the SPR sensor is much larger than that of the LSPR sensor, a study was performed using Ag nanoparticles with various out-of-plane heights but fixed in-plane widths. Nanoparticle arrays with out-of-plane heights of 16, 25, and 50 nm were fabricated. The mannose-functionalized nanoparticle arrays were placed in a flow cell with PBS buffer solution, then 19 μM ConA was injected, followed by rinsing with buffer to remove weakly bound ConA. Mannose-functionalized Ag nanosensors with 16 nm (Figure 5A), 25 nm (Figure 5B), and 50 nm (Figure 5C) out-of-plane heights gave shifts of 22.2, 11.4, and 6.7 nm when exposed to 19 μM ConA and 19.1, 9.6, and 5.8 nm overall responses when weakly bound ConA was
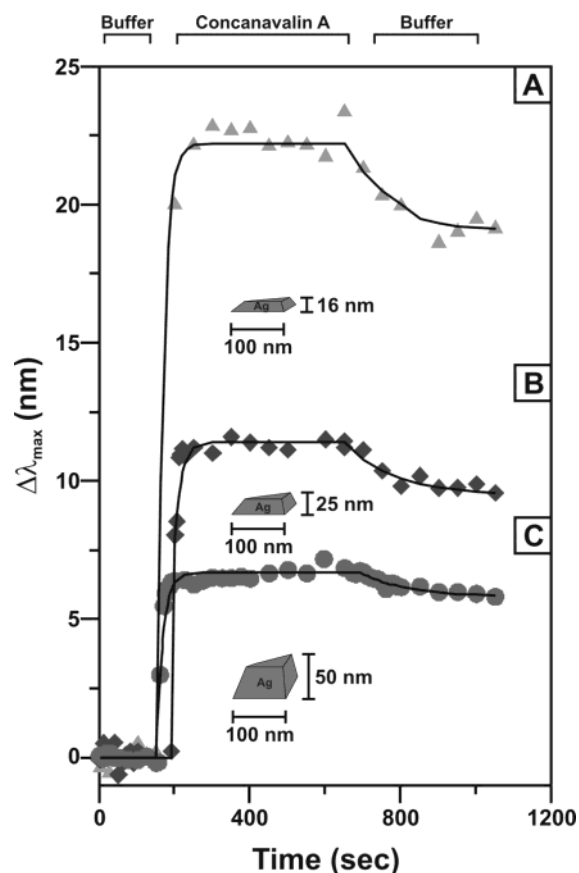
Figure 5. Real-time response of mannose-functionalized Ag nanosensor as 19 µM ConA was injected in the cell following buffer injection. (A) 16-nm out-of plane height, (B) 25-nm out-of plane height, and (C) 50-nm out-of-plane height. The solid lines are guides to the eye.

removed by washing the sample with the PBS buffer, respectively. In all cases, the density per unit area of ConA molecules bound to the mannose-functionalized surface was the same; however, with the decrease in the nanoparticle height, the overall response of the nanosensor increased. Also, when the ConA bound nanosensors were rinsed with buffer, the change in the response increased as the nanoparticle height decreased.

Electrodynamic Modeling. To explore the mechanism behind the experimental results in Figure 5, the discrete dipole approximation (DDA) method[45−47] was used to model the above experiments. In this application of the DDA method, the target particle and the surrounding layers of adsorbed molecules (SAM and ConA) are divided into a cubic array of N polarizable dipoles, with the polarizability of each element determined by the dielectric constant at the location of the dipole. The coupling of each dipole to the applied plane wave field and to the other dipoles is then described by solving $3N$ coupled dipole equations, and the extinction spectrum of the system is determined from the resulting induced polarizations at each dipole. This leads to a nearly exact solution of the electrodynamics of the particle and the adsorbed molecules, provided the array spacing is small enough. Here, the length of each cube is taken to be 1 nm, which is small enough to ensure convergence of the results. Additional assumptions in the calculations are that the molecules

(45) Draine, B. T.; Flatau, P. J. *J. Opt. Soc. Am. A* **1994**, 1491−1499.
(46) Draine, B. T.; Flatau, P. J. *User Guide for the Discrete Dipole Approximation Code DDSCAT.6.0*, 2003, http://arxiv.org/abs/astro-ph/0309069.
(47) Kelly, K. L.; Coronado, E.; Zhao, L.; Schatz, G. C. *J. Phys. Chem. B* **2003**, *107*, 668−677.

coat the exposed surface of the nanoparticles with layers with a uniform thickness that is specified below. This treatment was successfully used in earlier studies;[27,48] however, an additional feature of the present study is that the adsorbate layer structure consists of an SAM as the first layer and ConA as the second layer. Some of the ConA in the second layer is weakly adsorbed and can be removed by rinsing.

For the structural model, a typical silver particle is represented as a truncated tetrahedron with an in-plane width of 100 nm and an out-of-plane height of 16, 25, or 50 nm. The dielectric constant of silver is taken from Hunter and Lynch,[49] and the index of refraction of the 2-nm thick SAM is 1.463.[42] Note that the 2-nm layer thickness is an overestimate that is forced on us by the discrete size of the DDA cubes. DDA calculations for the SAM coated particle (height = 16 nm) lead to a λ_{max} of 817.9 nm, which is very close to the experimental result (λ_{max} = 810 nm). For calculations that include the ConA layer, the average thickness of the ConA is assumed to be 8 nm, which is close to the experimental value 7.7 nm (Figure 2). Calculations for a particle (height = 16 nm) with monolayer SAM and ConA yields a λ_{max} of 837.8 nm, resulting in a 19.9-nm red-shift due to the ConA. This value is very close to the experimental shift of 22 nm (Figure 5).

The dissociation phase SPR results (Figure 4A) indicate that 60% of the weakly adsorbed molecules are removed from the planar surface, whereas only a 14% LSPR shift is seen in the case of the LSPR sensor. To study this result, four structural models were studied: (1) model 1 assumes that removal of the adsorbed ConA leads to a layer that is still 8-nm thick in which the dielectric constant of the layer is the weighted average of the dielectric constants of ConA and water, with the weighting being determined by the coverage that is estimated by the SPR experiment. (2) In model 2, a fraction of the adsorbed 8-nm cubic ConA is randomly removed and DDA calculations on the partially coated system are performed. (3) In model 3, it is assumed that removal of some ConA allows for the remaining proteins to be packed more tightly around the SAM-coated nanoparticles. These calculations were therefore done with thinner, but uniformly covered, layers of ConA, with the layer thickness being determined by the coverage. (4) Model 4 assumes that removal of ConA occurs preferentially on the topmost surface of the nanoparticles and then proceeds down the nanoparticle sides. Thus, a fraction of the proteins is removed from top to bottom to determine the dependence of plasmon wavelength shift on coverage.

Figure 6 presents the wavelength shifts as a function of coverage for the four models, all for the height = 16 nm particle. This shows a linear dependence of shift on coverage for models 1 and 2, with nearly the same results for the two models. This is the result that is assumed to be appropriate for SPR experiments, but it clearly does not match the observed LSPR measurements. The results for models 1 and 2 also confirm that the effective medium theory is an accurate approximation when the partial coverage is achieved by random removal of ConA. Previously, we demonstrated that the wavelength shift for a truncated tetrahedron depends strongly on where the adsorbed molecules are located.[27] Molecules close to the sharp points near

(48) Haes, A. J.; Zou, S.; Schatz, G. C.; Van Duyne, R. P. *J. Phys. Chem. B* **2004**, *108*, 6961−6968.
(49) Lynch, D. W.; Hunter, W. R.; Palik, E. D. *Handbook of Optical Constants of Solids*; Academic Press: New York, 1985.
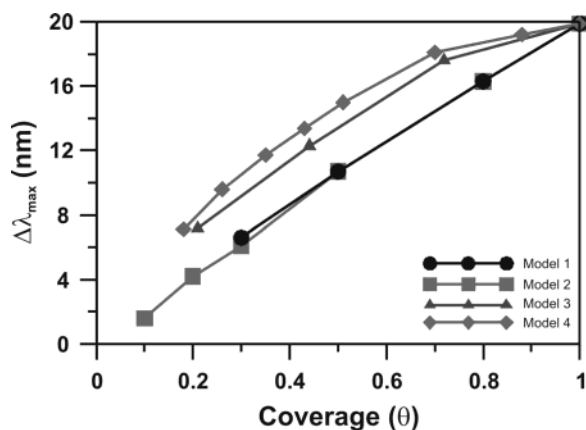
Figure 6. Wavelength shift as a function of coverage for the four models (out-of-plane height =16 nm Ag): (1) model 1 (effective medium approximation); (2) model 2 (random removal of molecules); (3) model 3 (adsorbate removal involves uniform restructuring to a thinner layer), (4) model 4 (preferential removal of adsorbates from the top of the particle)

the base of the particle (electromagnetic hot spots) experience much larger shifts than those on the flat regions. In addition, the shifts decrease in magnitude more rapidly with distance from the nanoparticle surface near the hot spots than elsewhere. Coincidently, for a uniform monolayer, the observed shift is an average over all hot and cool regions around the particle, and there is also some averaging over the distance from the surface that occurs for molecules that are 8 nm in thickness. Models 1 and 2 result in the random removal of ConA from the layer or using an effective medium to define a partially depleted layer, which leads to the results that are insensitive to the detailed structure of the electromagnetic field around the nanoparticle.

However, the results seen in models 3 and 4 are quite different from models 1 and 2, with a nonlinear dependence of wavelength shift on coverage in which the shift more quickly approaches its full monolayer result. For model 3, when the coverage of ConA is decreased from 100% to 40%, the plasmon wavelength shift changes from 19.9 to 11.5 nm (42%). This change is smaller than the 60% obtained from models 1 and 2, and yet, it does not match the experimental value of 14%. For model 4, when the coverage decreases from 100% to 40%, strong nonlinear dependence on coverage is seen with the plasmon wavelength shift changing from 19.9 to 12.7 nm (36%). Although the calculated value differs from the experimental result, this behavior is qualitatively correct. When removal of protein leads to a change in layer structure, either a thinner layer or a nonuniform layer, then the dependence of wavelength shift on coverage is nonlinear, which is in agreement with the experiment.

Plasmon shift calculations for nanoparticles with out-of-plane heights 25 and 50 nm were then carried out using model 4. The $\Delta\lambda_{max}$ was 14.6 and 12.7 nm for these Ag nanoparticles when the SAM-functionalized surface was fully covered with protein. The calculated $\Delta\lambda_{max}$ are in qualitative agreement with the experimental results: 11.4 and 6.7 nm.

Further, the effect of varying protein coverage on the wavelength shift for the 16-, 25-, and 50-nm particles was studied using model 4 (Figure 7). Increasing the particle height leads to stronger nonlinear behavior in which the percentage change in going from 40% to 100% coverage is smaller. For the 16 nm particle, the plasmon wavelength shift reduces by
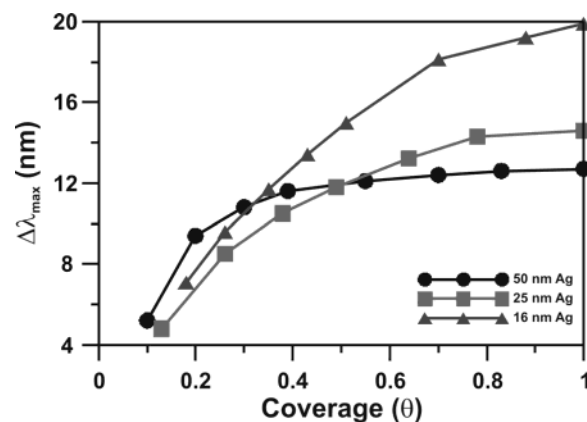
Figure 7. Wavelength shift versus protein coverage for Ag nanoparticles with out-of-plane heights of 50, 25, and 16 nm. Results presented are based on model 4.
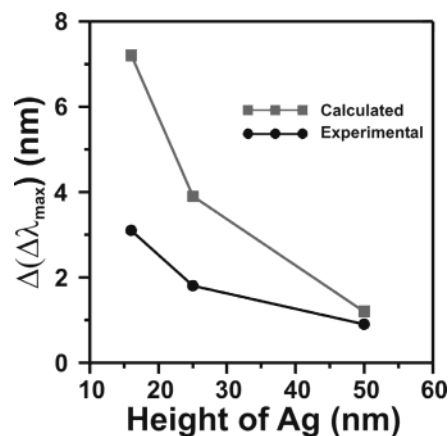
Figure 8. Comparison of theoretical calculated vs experimental values of change in wavelength shift vs Ag nanoparticle height at 40% ConA coverage.

7.2 nm when the coverage of the particle is changed from 100% to 40%, while the 25-nm particle shows a 3.9-nm decrease, and the 50 nm particle, a 1.2-nm decrease.

Figure 8 illustrates the correlation between theoretical calculations and the experimental values of the height of the nanoparticles and the change of $\Delta\lambda_{max}$. The circles (●) and squares (■) represent the $\Delta(\Delta\lambda_{max})$ obtained by subtracting $\Delta\lambda_{max}$ before and after the buffer rinse of the ConA bound surface for 16-, 25-, and 50-nm tall Ag nanoparticles for experimental and theoretical data, respectively. The values show qualitative agreement between theoretical calculated and experimentally observed data; as Ag nanoparticle height increases, decreasing the aspect ratio of the nanoparticle, the $\Delta(\Delta\lambda_{max})$ decreases. The discrepancy seen between the theoretically modeled values and experimental results is partially attributed to solvent annealing of the samples during the experiments. It has been previously shown that the annealed samples are less sensitive to the changes in the refractive index of the surrounding than the samples that are not annealed.[27] The trends presented in Figure 8 can be also explained using the l_d of the nanoparticle. Although the electromagnetic fields around the nanoparticles are known to be more complex, for an in-plane width of ~100 nm and out-of-plane height of ~50 nm for Ag nanoparticles, the well-approximated characteristic l_d is about ~5−6 nm.[20,50] Since the aspect ratio of the nanoparticle increases, the l_d of the Ag nanotriangles increases. As the
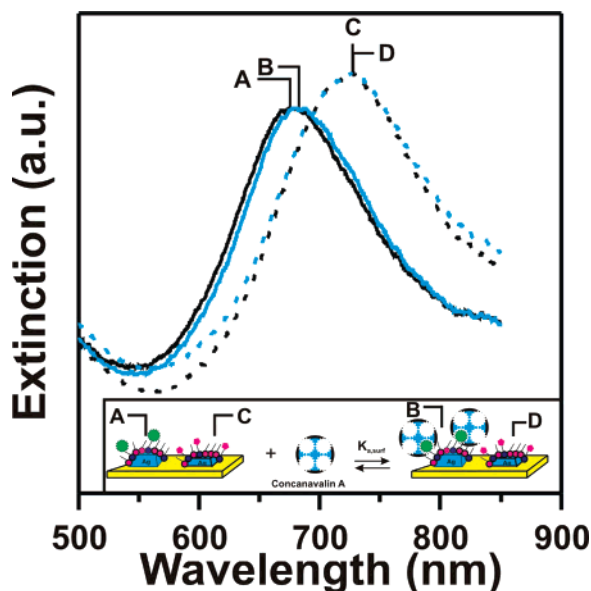
Figure 9. LSPR spectra illustrating multiplexing Ag nanosensor carbochip. Ag nanobiosensor with 35 nm Ag and 75 nm Ag were fabricated using NSL. (A) Ag nanoparticles (height = 75 nm) after 5 mM mannose modification, λ_{max} = 677.7 nm. (B) Ag nanoparticles (height = 75 nm) after exposure to 19 μM ConA, λ_{max} = 682.7 nm. (C) Ag nanoparticles (height = 35 nm) after 5 mM galactose modification, λ_{max} = 724.5 nm. Ag nanoparticles (height = 35 nm) after exposure to 19 μM ConA, λ_{max} = 724.6 nm. Inset shows the schematic of selective ConA binding to the mannose-functinalized portion of the carbochip.

characteristic l_d's of the nanoparticles are smaller than the size of ConA, the ConA bound on the surface may only be partially detected by the LSPR sensor. Conversely, the characteristic l_d for the SPR is known to be ~200 nm,[42] which results in a larger response change for SPR sensors when the weakly bound ConA was removed by washing the surface with buffer.

Although we are unable to distinguish between models 3 and 4 in the comparison to the experimental results, the data clearly show that there is sensitivity in the measured response to the distribution of protein around the particle surface. In both models 3 and 4, the first proteins removed are from cool regions (i.e., top of the surface) around the particle (with model 3 involving regions that are farther away from the surface of the particle and model 4 involving regions that are on the top surface of the particle). Either way, this leads to a smaller wavelength shift than one would obtain from random removal, which explains why the LSPR results are significantly different from SPR results. In addition, the first proteins removed from the taller particles have a smaller effect than shorter particles, resulting in a greater disparity between the effects of cooler and hotter regions for taller particles.

Fabrication of a LSPR Carbohydrate Sensing Chip. A (2 × 1) LSPR carbohydrate sensing chip sensor was fabricated by NSL. It consists of a glass substrate with nanoparticle arrays of two different heights (viz. 35 and 75 nm). The nanoparticle arrays were incubated in a solution of **1** and **2** to form a 5% malemide terminated SAM. The LSPR carbohydrate sensing chip was incubated in galactose and mannose thiol solutions resulting in an LSPR λ_{max} of 724.5 and 677.7 nm, respectively. To prevent the mixing of the sugar thiol solutions, the nanoparticle array elements were separated by a poly(dimethyl siloxane) mask. The galactose- and mannose-functionalized carbohydrate sensing chip was exposed to 19 μM ConA and

rinsed with PBS buffer resulting in an LSPR λ_{max} of 724.6 and 682.7 nm (Figure 9). When ConA binds to the mannose-functionalized surface, a 5-nm (682.7−677.7 nm) shift is seen, and when the ConA binds to the galactose-functionalized surface, a 0.1-nm (724.6−724.5 nm) shift is observed indicating that no binding occurs. The decrease in the LSPR shift seen when ConA binds to the mannose-functionalized Ag nanosensor with an out-of-plane height of 75 nm is attributed to the lower refractive index sensitivity of taller nanoparticles.[27,51] The inset shows the schematic of ConA binding to the sugar-functionalized nanoparticle arrays.

Conclusions

In this work, we have compared the responses of a planar, thin film Au SPR sensor with an NSL-fabricated Ag nanoparticle LSPR sensor using the binding of ConA to a mannose-functionalized SAM surface. Real-time angle shift SPR and wavelength shift LSPR measurements exhibited comparable magnitude saturation coverage responses during the association phase when ConA specifically bound to mannose ligand. On the other hand, during removal of weakly bound ConA during the dissociation phase, the SPR sensor showed approximately a 5 times greater response than the LSPR sensor. To verify that the response seen on the LSPR sensor was due to the specific binding of ConA to the mannose-functionalized Ag nanosensor, several nonspecific binding studies were performed. Neither Ery nor BSA bound to the mannose-functionalized Ag nanosensor. Additionally, an LSPR response was seen from a mixture of ConA and BSA. To understand the LSPR real-time response of the ConA binding to the mannose-functionalized surface, Ag nanoparticles with 16-, 25-, and 50-nm out-of-plane heights were constructed. The Ag nanoparticles with larger aspect ratios showed larger dissociation responses than Ag nanoparticles with smaller aspect ratios. A theoretical modeling using the DDA method and assuming that either ConA is removed from top to bottom of the surface of the nanoparticle or it is removed from outside to inside indicated that the long range of the electromagnetic fields surrounding Ag nanoparticles with large aspect ratios showed a greater dissociation response than Ag nanoparticles with smaller aspect ratios. Finally, this work demonstrates the first multiplexed version of an LSPR carbohydrate sensing chip to study the affinity of ConA on the mannose- and galactose-functionalized surface.

Future work will focus on fabricating carbohydrate sensing chips with multiple sugar arrays to investigate the binding of several proteins of interest simultaneously on a single chip. In addition, because LSPR sensors are inherently dependent upon single nanoparticles, they can be transitioned into in situ sensing in biological media.

(50) Jensen, T.; Kelly, L.; Lazarides, A.; Schatz, G. C. *J. Cluster Sci.* **1999**, *10*, 295−317.
(51) Jensen, T. R.; Malinsky, M. D.; Haynes, C. L.; Van Duyne, R. P. *J. Phys. Chem. B* **2000**, *104*, 10549−10556.